

Article

# Effect of Mg Contents on Catalytic Activity and Coke Formation of Mesoporous Ni/Mg-Aluminate Spinel Catalyst for Steam Methane Reforming

Hyunjoung Kim <sup>1,†</sup> , Young-Hee Lee <sup>1,†</sup>, Hongjin Lee <sup>1</sup>, Jeong-Cheol Seo <sup>2</sup> and Kyubock Lee <sup>1,\*</sup> 

<sup>1</sup> Graduate School of Energy Science and Technology, Chungnam National University, 99 Daehak-ro, Yuseong-gu, Daejeon 34134, Korea; ndieazure@o.cnu.ac.kr (H.K.); 201730154@o.cnu.ac.kr (Y.-H.L.); lhj15999@o.cnu.ac.kr (H.L.)

<sup>2</sup> Department of Chemical and Biomolecular Engineering, Korea Advanced Institute of Science and Technology, 291 Daehak-ro, Yuseong-gu, Daejeon 34141, Korea; sjc9201@kaist.ac.kr

\* Correspondence: kyubock.lee@cnu.ac.kr; Tel.: +82-48-821-8610; Fax: +82-42-821-8839

† These authors contributed equally to this work.

Received: 12 June 2020; Accepted: 21 July 2020; Published: 23 July 2020



**Abstract:** Ni catalysts are most suitable for a steam methane reforming (SMR) reaction considering the activity and the cost, although coke formation remains the main problem. Here, Ni-based spinel catalysts with various Mg contents were developed through the synthesis of mesoporous Mg-aluminate supports by evaporation-induced self-assembly followed by Ni loading via incipient wetness impregnation. The mesoporous Ni/Mg-aluminate spinel catalysts showed high coke resistance under accelerated reaction conditions (0.0014 g<sub>coke</sub>/g<sub>cat</sub>·h for Ni/Mg<sub>30</sub>, 0.0050 g<sub>coke</sub>/g<sub>cat</sub>·h for a commercial catalyst). The coke resistance of the developed catalyst showed a clear trend: the higher the Mg content, the lower the coke deposition. The Ni catalysts with the lower Mg content showed a higher surface area and smaller Ni particle size, which originated from the difference of the sintering resistance and the exsolution of Ni particles. Despite these advantageous attributes of Ni catalysts, the coke resistance was higher for the catalysts with the higher Mg content while the catalytic activity was dependent on the reaction conditions. This reveals that the enhanced basicity of the catalyst could be the major parameter for the reduction of coke deposition in the SMR reaction.

**Keywords:** steam methane reforming; spinel catalyst; Mg-aluminate; coke resistance; mesopore; basicity

## 1. Introduction

With the increasing concerns about air pollution and global warming, the development of a clean and alternative energy source to depleting fossil fuels has drawn great attention. Hydrogen, with strengths such as cleanness and high energy content, has been considered to be one of the most promising energy carriers [1]. Although the eventual method of hydrogen production should be renewable or low-carbon, such as via electrolysis of water, it is still highly costly and the majority of hydrogen production is based on fossil fuels. Steam methane reforming (SMR) is the most common and successful process of hydrogen production from natural gas, accounting for 76% of hydrogen production worldwide [2]. From the viewpoint of energy resources, the production of hydrogen from natural gas can be a smooth transition from fossil fuel-based energy system to renewable counterpart. Various transition-metal-based catalysts have been developed as SMR catalysts, including Pt, Rh, Ru, Pd, and Ni [3–6]. Considering the activity and the cost, Ni catalysts are regarded to be the most suitable, and the commercial SMR catalyst is Ni-based as well. Although it is a highly matured process, coke formation is still a main problem for the SMR reaction, together with sintering, which easily leads to the deactivation of catalysts [7,8].

Several strategies to solve the above-noted problems include developing catalysts with strong metal-support interaction (SMSI), high basicity, highly dispersed and small-size Ni crystals, and large surface area with high porosity [9–11]. First, catalysts with SMSI are known to maintain high dispersion of active metals with high resistance against sintering, which is also effective for inhibiting carbon formation [12–15]. For example, Ni<sub>0.5</sub>Mg<sub>2.5</sub>AlO<sub>9</sub> catalysts prepared by the co-precipitation method showed, compared with Ni catalysts prepared by impregnation, SMSI and higher activity for SMR into syngas with higher resistance against sintering and coke formation [14]. In a study of Han et al., SMSI mediated by magnesium addition well maintained Ni dispersion with a particle size of 2.6 nm for dry methane reforming (DMR) [16]. Second, increasing the basicity of a catalyst is known to be an effective way of suppressing carbon deposition in reforming reactions, since carbon is easily formed from CH<sub>4</sub> decomposition on acidic surfaces [17–19]. Combining alkaline earth metals/metal oxides such as MgO and CaO on an Al<sub>2</sub>O<sub>3</sub> support is a widely employed means of enhancing Ni catalyst basicity [19,20]. Koo et al. studied the promotion of MgO on Ni-based alumina catalysts for combined steam and carbon dioxide reforming of methane (CSCRM) [17]. They found that 20 wt% MgO effectively suppressed coke formation with enhanced catalytic activity due to the increased CO<sub>2</sub> adsorption and SMSI. Third, improving the dispersion of an Ni catalyst of minimum size on a support increases highly active reaction sites [19]. In this regard, positioning Ni metals in the interconnected pores of a support is crucial as it not only provides highly accessible Ni-active centers, but also plays an important role in stabilizing Ni nanoparticles by the confinement effect [21,22]. In the preparation of catalysts using the incipient wetness impregnation method, the uniformity, size, and dispersion of the active metal is directly determined by the porosity of the support. Considering the uniformity and size of active metal, well-defined and ordered mesopores are highly desirable. In summary, for the rational design of Ni-based SMR catalysts, optimization of the following three catalytic parameters is crucial: (1) SMSI, (2) basicity, and (3) porosity.

The MgAl<sub>2</sub>O<sub>4</sub> spinel structure has been used as a catalyst and catalyst support in various chemical reactions due to its high thermal stability, excellent chemical stability, mechanical strength, and surface basicity [23]. Compared with commonly used alumina, Ni-loaded MgAl<sub>2</sub>O<sub>4</sub> has shown high coke resistance in SMR, DMR and CSCMR reactions [18,24–27]. The effects of the Mg(Ca) content on the basicity, Ni crystal size, and pore size of the Ni-Mg(Ca)-Al oxides catalyst have been widely studied [28–30]. The main reason for reduced coke deposition is the improved basicity and dispersion of the Ni particles on the support, resulting in SMSI. This leads to development of mesoporous MgAl<sub>2</sub>O<sub>4</sub>, especially with highly ordered mesopores [31–33]. Rezaei et al. synthesized mesoporous MgAl<sub>2</sub>O<sub>4</sub> by a surfactant-assisted co-precipitation method using triblock copolymer as a surfactant followed by Ni impregnation for DMR [32]. Mesoporous nanocrystalline MgAl<sub>2</sub>O<sub>4</sub> as a support for Ni catalysts are prepared via a simple sol-gel route for biogas reforming by the same group [31]. Ni-loaded MgAl<sub>2</sub>O<sub>4</sub> with more well-defined and highly ordered mesopores was prepared by the evaporation-induced self-assembly (EISA) method using structure guiding agents (SDA) as sacrificial templates, and used for CO<sub>2</sub> methanation [33]. Compared with alumina- or silica-based materials, it has proved difficult to obtain well-defined mesopores formed by SDA with high thermal stability in cases of MgAl<sub>2</sub>O<sub>4</sub>, owing to sintering-driven deformation starting from around 700 °C while the optimum reaction temperature of SMR is in the range of 750–800 °C. We recently found that Mg-aluminate with higher resistance against sintering could be obtained with the defect spinel structure [34].

In this study, we investigate the effect of the Mg content on the Ni crystal size, the pore structure, the basicity of the catalysts, and the resulting catalytic activity and coke resistance of the mesoporous Ni/Mg-aluminate spinel catalyst in SMR reaction. The mesoporous Mg-aluminate supports were synthesized by the EISA method, and active sites were loaded by incipient wetness impregnation of Ni. The Mg/Al molar ratio was adjusted to 0.10, 0.23, 0.32 and 0.43 while fixing Ni contents to be 15 wt%. In order to understand the resistance of catalysts against coke formation, the SMR reaction was performed under accelerated deactivation conditions. Especially, we try to understand the effect

of the Mg contents on the physicochemical properties of the spinel catalysts from viewpoints of the sintering resistance and the Ni particle formation by the exsolution, which has been less studied before.

## 2. Results and Discussion

Figure 1 shows TEM images of Mg-aluminates calcined at 900 °C. In the case of Mg9 and Mg19 with low Mg content (Mg/Al molar ratios of 0.10 and 0.23, respectively), well-defined and ordered mesopores formed by decomposition of the self-assembled P123, namely SDA, were clearly observed (Figure 1a,b). The insets in Figure 1a,b show line-scanned profiles displaying the width of pores and walls with regularity. The averaged pore sizes were measured to be 14.09 nm and 16.84 nm for Mg9 and Mg19, respectively. However, in the case of Mg25 and Mg30 with higher Mg content (Mg/Al molar ratios of 0.32 and 0.43, respectively), no well-defined or ordered mesopores were found (Figure 1c,d). As shown in TEM images of Supplementary Figure S1, well-defined and ordered mesopores were maintained regardless of Mg content in the case of Mg-aluminate calcined at 600 °C. This means that well-defined and ordered mesopores of Mg-aluminate with high Mg content (Mg25 and Mg30) were collapsed by sintering below 900 °C. The Mg/Al molar ratio of Mg30 is close to that of the  $\text{MgAl}_2\text{O}_4$  spinel phase. Koo et al. reported severe sintering of  $\text{MgAl}_2\text{O}_4$  as a catalyst support with the increase of calcination temperature from 800 to 1200 °C [18]. A similar trend was observed with their Ni-loaded catalysts. The BET surface area, in that study, decreased gradually from 108 to 15  $\text{m}^2/\text{g}$ , while the crystallite size of Ni- $\text{MgAl}_2\text{O}_4$  increased from 4 to 53 nm under 800–1200 °C calcination.

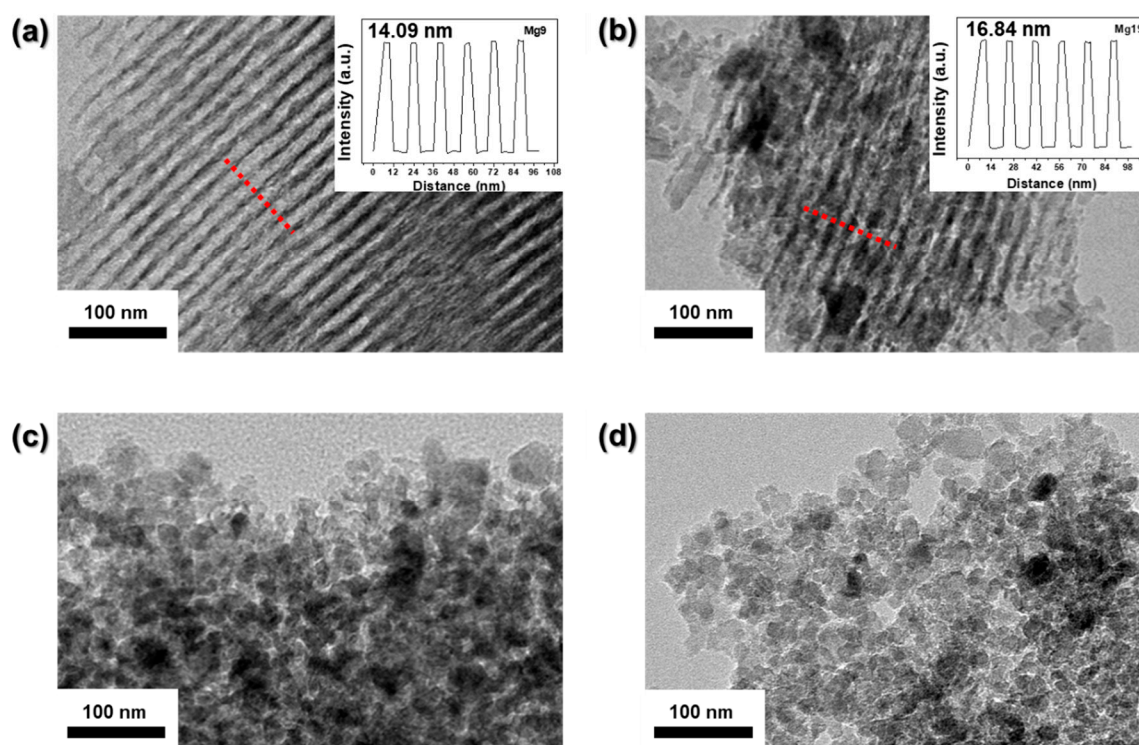


**Figure 1.** TEM images of mesoporous Mg-aluminate support calcined at 900 °C: (a) Mg9, (b) Mg19, (c) Mg25, (d) Mg30.

The change of the pore structures of the Mg-aluminates by sintering in the present study was confirmed by BET and BJH analysis (Figure 2). There was a very clear trend of decreasing BET surface area and increasing pore size with increasing Mg content or Mg/Al ratio (Figure 2 and Table S1 in the Supplementary Materials). In Figure 2a, the  $\text{N}_2$  adsorption-desorption isotherms of all of the supports show typical mesopore type IV hysteresis curves. The mesoporous supports could be classified in more detail by the Langmuir theory. The hysteresis loop was close to the H1 type, facile pore connectivity and high pore size uniformity, all of which reflect the typical pore-structure form by decomposition of

self-assembled P123 [19,33]. The pore size of mesoporous metal oxide prepared by the soft-templating method is dependent on the SDA. Previous studies show that, in the synthesis of alumina, triblock copolymer Pluronic F127 as the SDA generates smaller mesopores (4–7 nm) than those (upto 15 nm) formed by P123. Furthermore, surfactants such as cetrimonium bromide and sodium dodecyl sulfate as the SDA generate even smaller mesopores [35]. Considering mass transport, the catalyst support with larger mesopores would be more advantageous in the SMR reaction, which is the main reason why P123 is used in this study. The BJH plots in Figure 2b show the pore size distribution with narrow peaks between 6 and 20 nm. Smaller pores were formed for Mg-aluminate with lower Mg/Al ratio. As shown in the Table S1, the BET surface area was increased from 93 m<sup>2</sup>/g (Mg30) to 170 m<sup>2</sup>/g (Mg9). Interestingly, the pore volumes of the Mg-aluminates were similar regardless of the Mg/Al ratio (Supplementary Table S1). From these results, it can be inferred that the resistance against sintering is higher for Mg-aluminate with a lower Mg/Al ratio, and therefore, mesopores formed by decomposition of SDA are maintained better after calcination. On the other hand, for the Mg-aluminate with higher Mg/Al ratio, the nanocrystals were sintered to form enlarged intraparticle pores while the total pore volume maintained was similar. After Ni loading with calcination and after reduction, the BET surface area was decreased while the trend of BET surface area,  $d_p$  value, and mean pore size according to Mg contents were similarly maintained (Figure 2).

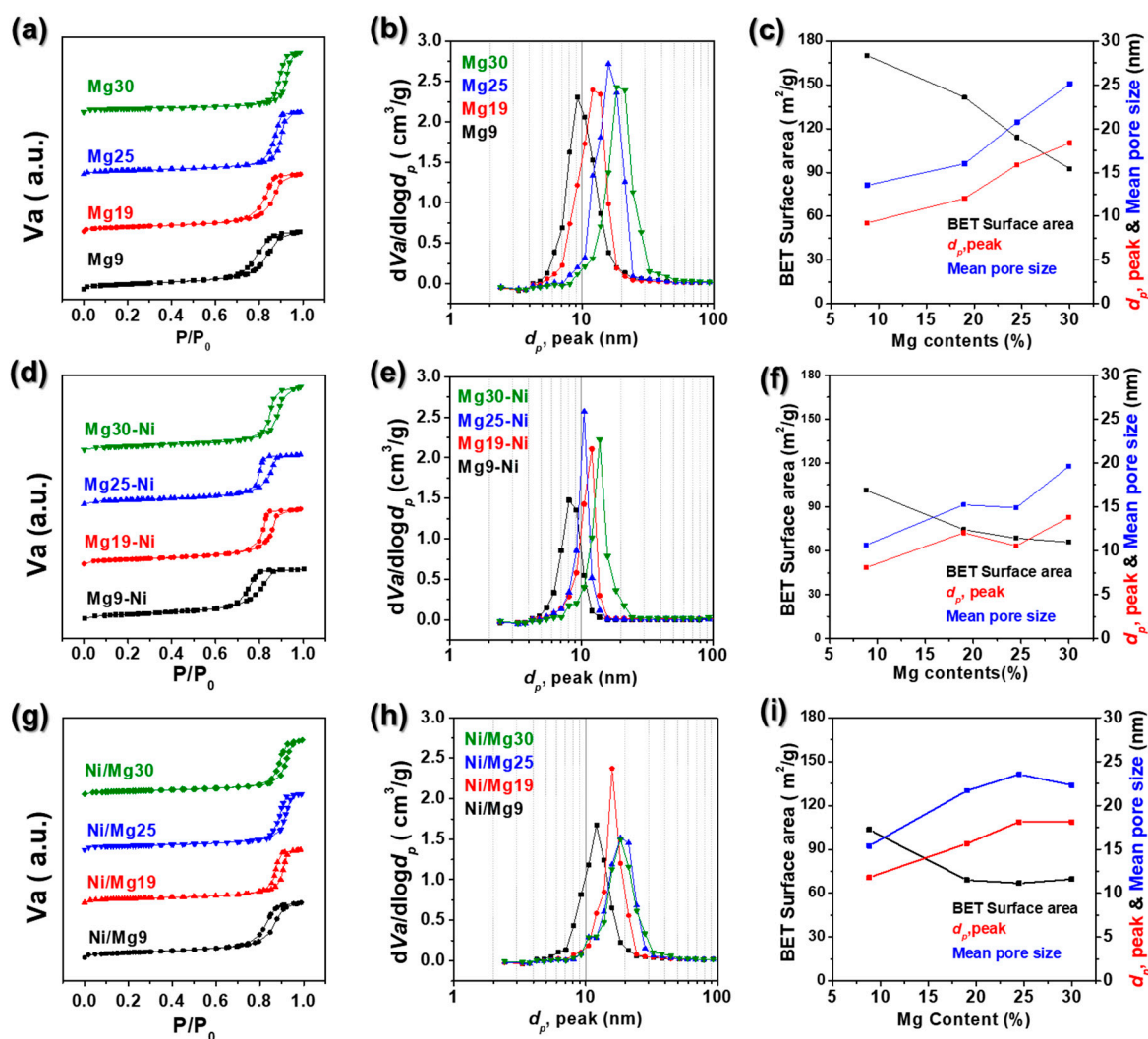


**Figure 2.** BET and BJH analysis of (a–c) Mg-aluminate support, (d–f) after Ni loading with calcination, and (g–i) after reduction: (a,d,g) N<sub>2</sub> adsorption-desorption isotherms, (b,e,h) BJH pore size distributions, and (c,f,i) plots of BET surface area,  $d_p$  value, mean pore size versus Mg contents.

The synthesized Mg-aluminate showed the spinel phase. The degree of sintering (or sintering resistance) of Mg-aluminate according to the Mg/Al ratio could be also confirmed by XRD (Figure 3a). The XRD pattern of Mg30 was close to that of  $\text{MgAl}_2\text{O}_4$  (JCPDS #21-1152, Supplementary Table S2). As the ratio of Mg/Al was lowered, the peaks were right shifted, and the XRD pattern of Mg9 was close to that of  $\text{Mg}_{0.388}\text{Al}_{2.404}\text{O}_4$ , which is known as the defect spinel phase (JCPDS #48-0528, Supplementary Table S2) [36]. The main cause of the high thermal stability of Mg9 and Mg19 against sintering, which leads to well-developed and ordered mesopores, as shown in Figure 1, is considered to be Mg deficiency at the octahedral sites of the spinel [36]. The peaks of Mg19 and Mg25 were between those of Mg9 and Mg30. This peak shift was observed more clearly for the peak of the (440) plane. For careful peak identifications, the peaks of the (440) plane were magnified as shown to the right of the XRD patterns in Figure 3. The 2-theta of the (440) plane decreased from 66.25 degrees for Mg9 to 65.35 degrees for Mg30.

After Ni impregnation into Mg-aluminate, NiO peaks were observed in the XRD patterns (Figure 3b). The ICP analysis shows that all the samples have equivalent Ni contents (Table 1). The peak intensity, however, decreased with decreasing Mg/Al ratio, and no peak was found in Mg9-Ni. The reason for the absence of an NiO peak in Mg9-Ni was the filling of Mg-deficient sites (A in  $\text{AB}_2\text{O}_4$ ) by Ni atoms to form the spinel  $\text{MgNiAl}_2\text{O}_4$  phase. On the other hand, Mg19, Mg25 and Mg30 had no or not enough defect sites of A in  $\text{AB}_2\text{O}_4$  to be filled by added Ni atoms, and therefore, surplus Ni atoms not included in the spinel matrix formed the NiO phase, as indicated in Figure 3b. It is notable that the diffraction peaks were left-shifted by Ni impregnation (Figure 3b,d). The width of the peak shift reflected the extent of A-site deficiency in the support samples or, equally, the amount of Ni filled into the impregnated samples. There was almost no peak shift for Mg30, and its width increased with decreasing Mg/Al ratio, which phenomenon inversely matched the intensity of the NiO peak.

After the reduction of the impregnated samples, Ni peaks were clearly observed, and the peaks of the spinel were right shifted, far more than even the pre-impregnation support. The crystallite size of Ni calculated using the Scherrer equation based on the peak at  $2\theta = 51.85^\circ$ , (200) plane was smaller along with lower Mg contents (Table 1). This is more evident with TEM observation (Figure 4 and Table 1). There have been several researches of Mg effect on the size of Ni in Ni-Mg-Al oxides [17,28–30]. Different from previous studies, the change of Ni crystal size by Mg content could be explained based on exsolution during reduction process. The right shift of the diffraction peaks was owed to exsolution of the Ni, which resulted in renewed A-site deficiency. In the spinel ( $\text{AB}_2\text{O}_4$ ) or perovskite ( $\text{ABO}_3$ ) structure, easily reducible cations at the A or B sites, respectively, were diffused out to the surface and formed metal nanoparticles under the reducing atmosphere, which effect is known as the exsolution process [37–39]. Here, the extent of exsolution or width of right shift was proportional to the width of left shift by Ni impregnation and the extent of A-site deficiency (Figure 3d). The peak shift of Mg30, again, was negligible (Figure 3c,d). The greater post-reduction right shift of the diffraction peak relative to the peak position of the support could be attributed to the partially exsolved Mg atoms in addition to the exsolved Ni atoms.

**Table 1.** ICP-AES analysis and the Ni particle sizes evaluated by XRD and TEM.

	ICP-AES			Ni Particle Size (nm)	
	Ni (wt%)	Mg (wt%)	Al (wt%)	XRD	TEM
<b>Ni/Mg9</b>	15.13	8.76	38.25	14.5	14.92 ± 2.11
<b>Ni/Mg19</b>	15.09	18.61	38.48	25.0	20.47 ± 2.46
<b>Ni/Mg25</b>	15.05	25.44	39.12	25.6	24.84 ± 2.84
<b>Ni/Mg30</b>	15.06	29.57	39.63	27.4	30.19 ± 2.25

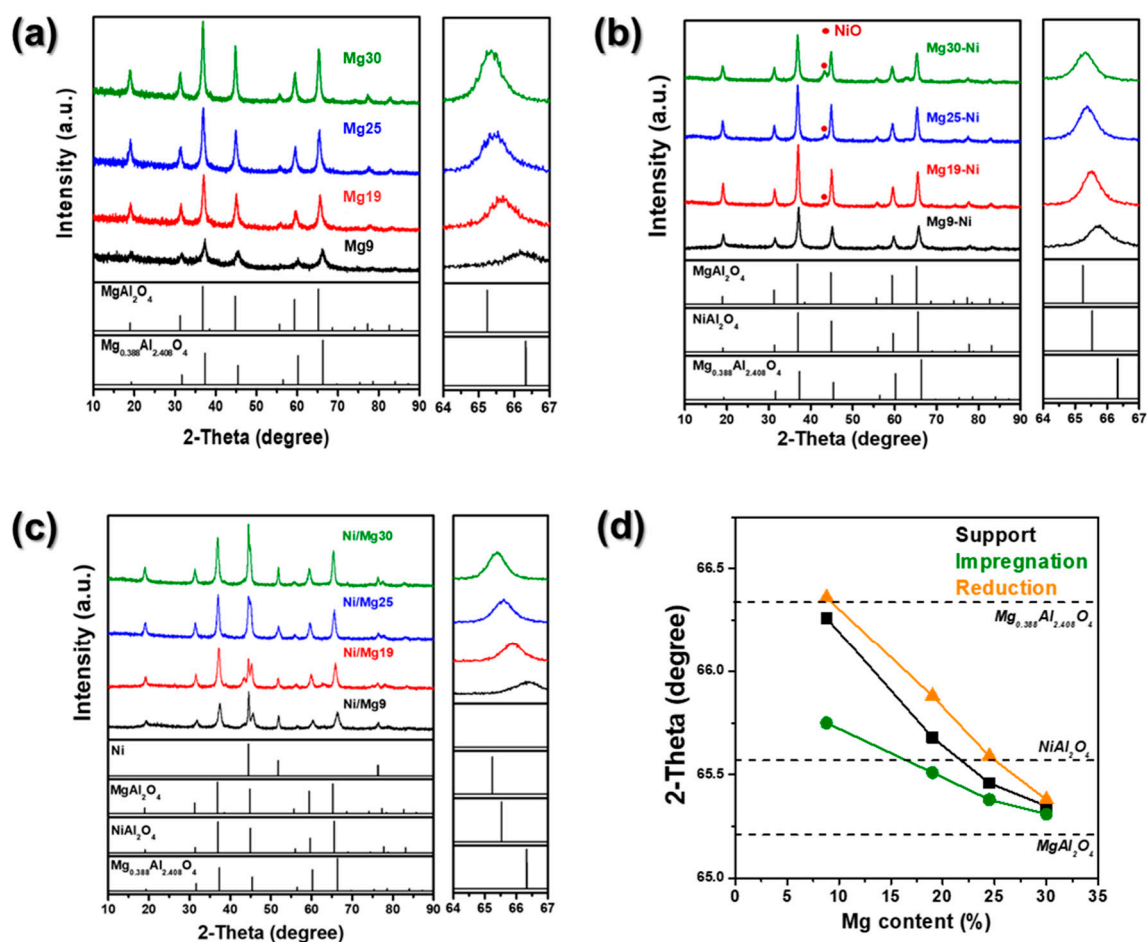


**Figure 3.** XRD analysis: (a) Mg-aluminate support, (b) after Ni loading with calcination, (c) after reduction, and (d) plots of 2-theta shift for (440) plane.

The  $H_2$ -TPR analysis revealed that there were two weak reduction peaks (the satellite peaks around 500 and 600 °C) and two strong peaks at around 750 and above 800 °C (Figure 5). The reduction peaks at around 500 and 600 °C were attributed to the reduction of bulk NiO species weakly interacting with the support. The peaks at around 750 °C could be attributed to the reduction of complex  $NiO_x$  species strongly interacting with the support [32,36]. The peaks above 800 °C were attributed to the reduction of  $NiAl_2O_4$  with or without MgO or CaO promotion, which was not observed only for Mg30-Ni [17,19]. This was due to the fact that Mg30 was stoichiometrically full, forming the  $MgAl_2O_4$  spinel structure. After Ni impregnation, Ni was not embedded into the A site, and therefore, the  $NiAl_2O_4$  phase was not formed. On the other hand, the peak at around 750 °C, attributable to NiO species reduction and strongly interacting with the support, was not observed only for Mg9-Ni. This is consistent with the XRD data in Figure 3b showing no evident NiO for Mg9-Ni, since all of the Ni atoms had been accepted into the A site to form the  $NiAl_2O_4$  phase. The order of peak intensity at around 750 °C was as follows: Mg30-Ni > Mg25-Ni > Mg19-Ni. This is in line with the trends of NiO peak size and extent of peak shift in the XRD patterns (Figure 3b,d).

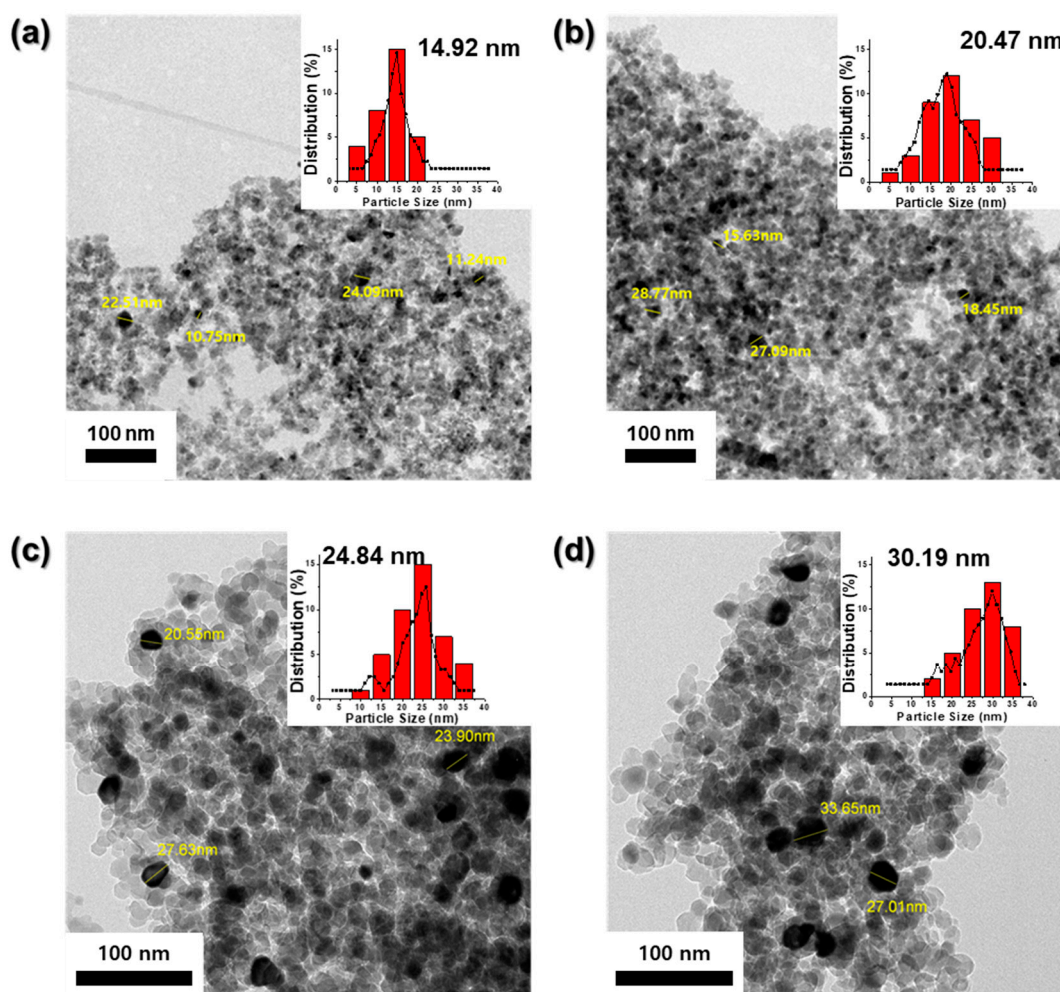


**Figure 4.** TEM images and Ni particle size distributions of (a) Ni/Mg9, (b) Ni/Mg19, (c) Ni/Mg25 and (d) Ni/Mg30 after reduction at 800 °C for 2 h.

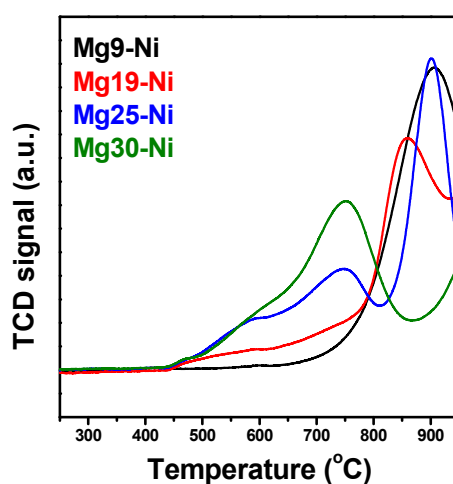


**Figure 5.** H<sub>2</sub>-TPR of Mg-aluminates after Ni loading with calcination.

Figure 6a shows the time-on-stream CH<sub>4</sub> conversion in the SMR reaction with increasing GHSV at 800 °C with a steam-to-carbon ratio (S/C) of 3. For comparison, a commercial catalyst was reacted under the same conditions. At the reaction temperature of 800 °C with S/C = 3, the calculated CH<sub>4</sub> conversions at the thermodynamic equilibrium is 100%. All catalysts except Ni/Mg9 reached the

thermodynamic equilibrium at the GHSV of  $8000\text{ h}^{-1}$ .  $\text{CH}_4$  conversion of 100% was maintained up to the GHSV of  $16,000\text{ h}^{-1}$  for the developed catalysts other than Ni/Mg9, whereas the commercial catalyst showed decreased conversion at the GHSV of  $16,000\text{ h}^{-1}$ . The  $\text{CH}_4$  conversions at the GHSV of  $24,000\text{ h}^{-1}$  were in the following order: Ni/Mg25 > Ni/Mg30 > Ni/Mg19 > Ni/Mg9 > commercial catalyst. At the higher GHSV, the more likely SMR will be controlled by diffusion phenomena. Ni/Mg25 and Ni/Mg30, having greater pore sizes (Figure 2 and Table S1), show higher activity at  $800\text{ }^\circ\text{C}$  than Ni/Mg9 and Ni/Mg19 with narrower pores. The carbon balance of the reaction follows the trend of  $\text{CH}_4$  conversion (Figure 6b). The  $\text{H}_2/\text{CO}$  ratios of Ni/Mg19, Ni/Mg25 and Ni/Mg30 at the GHSV of  $8000\text{ h}^{-1}$  were around 3.6, which were decreased at the GHSV of  $16,000\text{ h}^{-1}$  but still higher than 3 (Figure 6c). The higher  $\text{H}_2/\text{CO}$  ratio than 3, the theoretical  $\text{H}_2/\text{CO}$  ratio in SMR, reflects that there was a further reaction of water gas shift in the presence of excess water ( $\text{S}/\text{C} = 3$ ). The low CO selectivity at the low GHSV because of water gas shift is confirmed in Figure 6d. At the GHSV of  $24,000\text{ h}^{-1}$ ,  $\text{H}_2/\text{CO}$  ratios of Ni/Mg19, Ni/Mg25 and Ni/Mg30 are around 3 with increased CO selectivity.

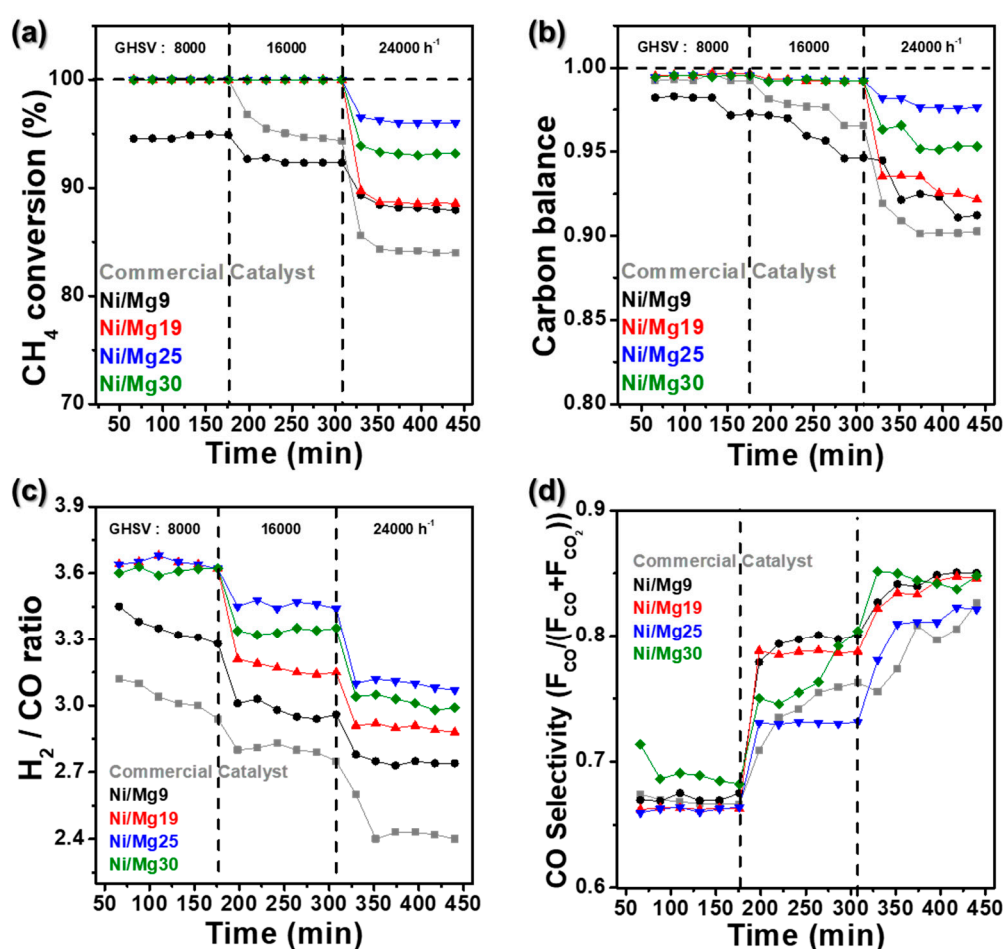


**Figure 6.** Time-on-stream result of SMR reaction with Ni/Mg-aluminate catalysts and commercial catalyst at  $800\text{ }^\circ\text{C}$  with different GHSV of 8000, 16,000, 24,000  $\text{h}^{-1}$ : (a)  $\text{CH}_4$  conversion, (b) carbon balance, (c)  $\text{H}_2/\text{CO}$  ratio, and (d) CO selectivity.

In order to understand the resistance of catalysts to coke formation, the SMR reaction was performed under accelerated deactivation conditions ( $\text{S}/\text{C} = 1$ ,  $\text{GHSV} = 8000\text{ h}^{-1}$ ,  $700\text{ }^\circ\text{C}$ ). In contrast to the results of  $\text{CH}_4$  conversion at  $800\text{ }^\circ\text{C}$  with  $\text{S}/\text{C} = 3$  (Figure 6), the conversion by Ni/Mg9 and Ni/Mg19 at  $700\text{ }^\circ\text{C}$  with  $\text{S}/\text{C} = 1$  was slightly higher than that by Ni/Mg25 and Ni/Mg30 (Figure 7a,b). However, the carbon balance was highest for Ni/Mg30, which resulted in the lowest coke formation in that catalyst (Figure 7b,c). The amount of deposited coke by TGA analysis was in accordance with the carbon

balance measured during the reaction (Figure 7b and Supplementary Figure S2), where the lower carbon balance reflects the more carbon consumption for the formation of coke. The  $H_2/CO$  ratio was not higher than 3 under the SMR reaction with  $S/C = 1$  where  $H_2O$  was not enough for water gas shift (Figure 7d). It is notable that the trend of decreasing coke deposition with increasing Mg content was clearly observed (Figure 7b). The amount of coke formed per gram of catalysts per hour was calculated to be 0.0050, 0.0046, 0.0040, 0.0034, and 0.0014  $g_{\text{coke}}/g_{\text{cat}} \cdot h$  for commercial catalyst, Ni/Mg9, Ni/Mg19, Ni/Mg25, and Ni/Mg30, respectively. The effect of increasing basicity by introduction of Mg or MgO to Ni-alumina-based catalysts on coke formation in SMR and DMR reactions has been reported [20,24]. At the surface of the catalyst, increased basicity reduces coke formation by forming surface-activated  $O^*$ , which can react with neighboring  $C^*$  and result in formation of CO and  $CO_2$  [19,40]. It is also widely accepted that smaller sized Ni particles with higher SMSI and higher dispersion of active sites shows higher coke resistance, and the developed catalysts with lower Mg show smaller Ni particles (Table 1 and Figure 4) [9,22]. Our results show that catalysts with higher Mg content and basicity show a more dominant effect than the effect of Ni particle size on suppressing coke formation.

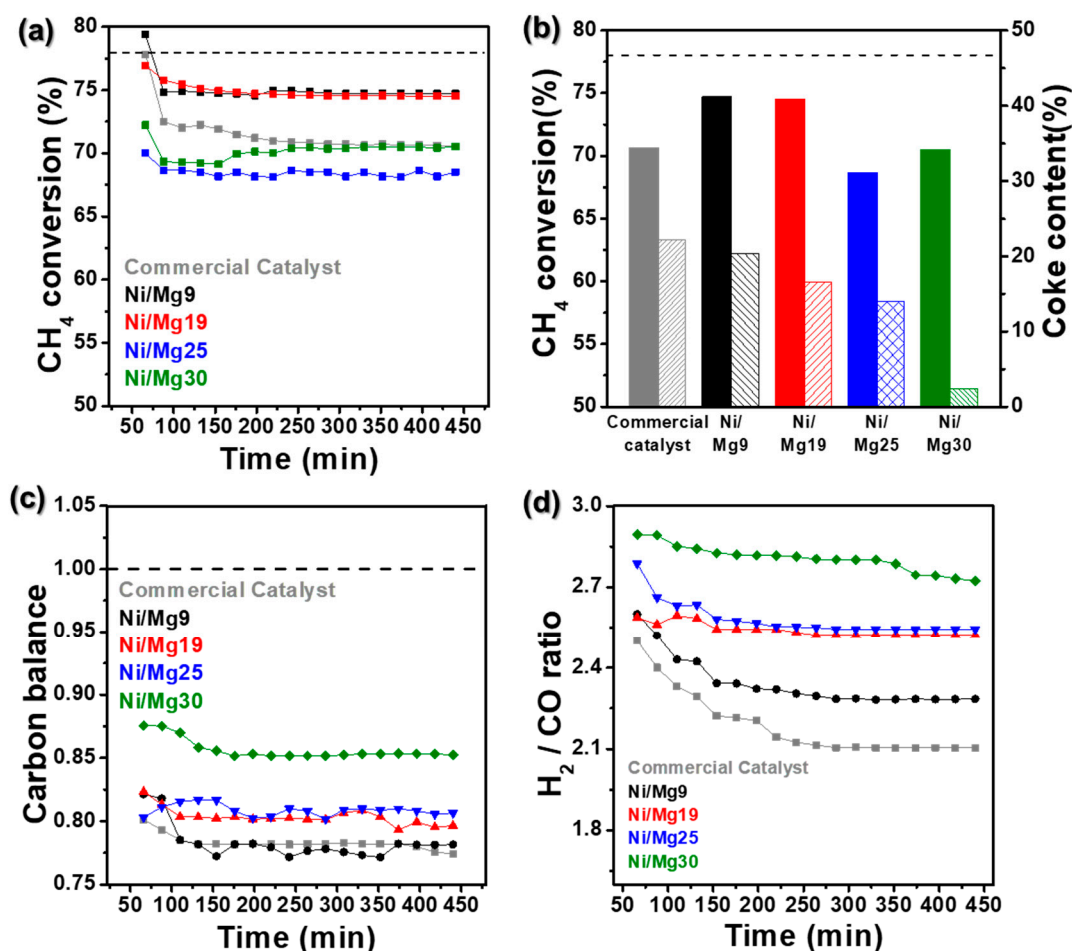


**Figure 7.** Time-on-stream result of SMR reaction under accelerated deactivation conditions at 700 °C and GHSV of 8000 h<sup>-1</sup> with S/C of 1: (a) CH<sub>4</sub> conversion, (b) averaged CH<sub>4</sub> conversion and coke contents measured by TGA analysis, (c) carbon balance, and (d) H<sub>2</sub>/CO ratio.

The CO<sub>2</sub>-TPD profiles in Figure 8 reveal the basicity of the catalysts. For all of the samples, two peaks of CO<sub>2</sub> desorption are shown at about 120 °C (low temperature, peak I) and 400 °C (high temperature, peak II). The amount of CO<sub>2</sub> desorbed is indicative of the number of basic sites on the catalyst [41]. The amount of CO<sub>2</sub> desorption calculated based on the total area of the CO<sub>2</sub>-TPD (peak I + peak II) increased with increasing Mg content, as shown in Table 2. Peak I at low temperature

originated from CO<sub>2</sub> desorption from the weak basic sites, and peak II, from the medium or strong basic sites [42]. The trend was very clear: the greater the Mg content, the greater the amount of CO<sub>2</sub> desorption from the medium/strong basic sites (Table 2). Furthermore, the ratio of peak II to peak I for Ni/Mg30 was more than double those of the others (Table 2). This confirms that the presence of Mg increased the basicity of the catalyst and increased the resistance to coke formation, which result is in good agreement with the amount of coke deposition as analyzed by TGA (Figure 7b and Supplementary Figure S2). Although Ni/Mg9 showed the highest surface area and smallest Ni particle size, which is typically advantageous for an Ni catalyst, Ni/Mg30 showed the highest coke resistance.

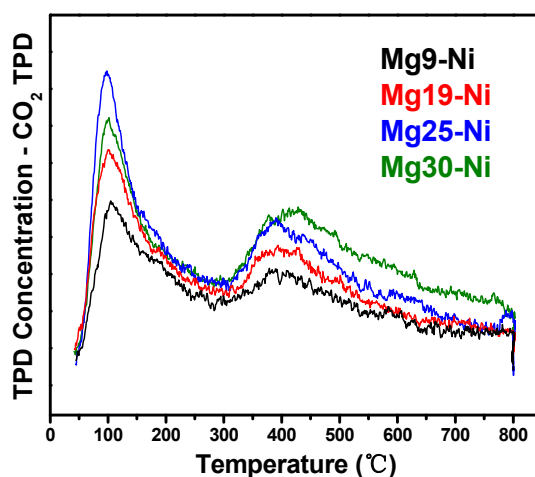


Figure 8. CO<sub>2</sub>-TPD profiles of Ni/Mg-aluminate catalysts.

Table 2. The amount of CO<sub>2</sub> desorption calculated based on CO<sub>2</sub>-TPD profiles of Ni/Mg-aluminate catalysts.

Peak-Fitting Data	Peak I mmol/g	Peak II mmol/g	Total mmol/g	Ratio of Peak II/I
Ni/Mg9	0.135387	0.062524	0.197911	0.46
Ni/Mg19	0.154042	0.075213	0.229255	0.48
Ni/Mg25	0.211875	0.107514	0.319389	0.51
Ni/Mg30	0.178361	0.199472	0.377833	1.11

### 3. Materials and Methods

#### 3.1. Materials

Aluminum iso-propoxide (Al(OiPr)<sub>3</sub>, ≥98%, Sigma-Aldrich, St. Louis, MO, USA) and magnesium dichloride (MgCl<sub>2</sub>, ≥98%, Sigma-Aldrich, St. Louis, MO, USA) were used as precursors for the synthesis of an Mg-aluminate support. Absolute ethanol (C<sub>2</sub>H<sub>5</sub>OH, OCI, Seoul, Korea) and nitric acid (HNO<sub>3</sub>, 60.0%, OCI, Seoul, Korea) were used as solvents. Pluronic P123 (EO<sub>20</sub>PO<sub>70</sub>EO<sub>20</sub>, Mw = 5800, Sigma-Aldrich, St. Louis, MO, USA) was used as the SDA. Nickel nitrate (Ni(NO<sub>3</sub>)<sub>2</sub>·6H<sub>2</sub>O, ≥98%, Sigma-Aldrich, St. Louis, MO, USA) was used as the Ni precursor. All of the chemicals were used as received without further purification.

#### 3.2. Preparation of Ni/Mg-Aluminate Catalysts

The EISA method was used to synthesize the catalyst supports [34]. The EISA method using self-assembled amphiphilic molecules as templates is a simple means of synthesizing metal oxides of mesoporous structure [19,36,37]. First, precursor was prepared by adding 6.57 g of P123 to a mixture of 135.0 mL of ethanol and 11.0 mL of nitric acid under vigorous stirring. Next, Al(OiPr)<sub>3</sub> and MgCl<sub>2</sub> were added to the P123-containing solution, which was stirred for a further 5 h. The mixing ratio of all of the components was fixed as (Al(OiPr)<sub>3</sub> + MgCl<sub>2</sub>):P123:EtOH:HNO<sub>3</sub> = 1:0.017:34.100:2.090.

The molar ratio of  $\text{MgCl}_2$  to  $\text{Al}(\text{OiPr})_3$  for Mg9, Mg19, Mg25, and Mg30 was 0.10, 0.23, 0.32, and 0.43, respectively. The precursor solution was oven-dried at 60 °C for 48 h. Then, calcination was carried out at 900 °C for 5 h in air to obtain the Mg-aluminate support in the form of white powder. Ni was loaded on the Mg-aluminate support by the incipient wetness impregnation method. The weight percent of Ni metal in the catalyst was fixed to be 15 wt%. The Ni-loaded Mg-aluminate was dried at 60 °C for 4 h, followed by calcination at 900 °C for 2 h. The obtained powder was pelletized under 200 bar, then ground and sieved to separate particles of 80–100 mesh size for the catalytic reaction. The sample nomenclature is as follows: 'Mg9' for support, 'Mg9-Ni' for Ni-impregnated and calcined sample, and 'Ni/Mg9' for reduced sample (also: Mg19, 25, 30).

### 3.3. Catalyst Characterization

X-ray diffraction (XRD) analysis was performed with an AXS D8 diffractometer (Bruker, Billerica, MA, USA) at Cu  $K\alpha$  wavelength, 40 kV, and 40 mA. The crystallite sizes of metallic Ni were calculated using the Scherrer equation based on the peak at  $2\theta = 51.85^\circ$ , (200) plane. The main peak of metallic Ni at  $2\theta = 44.51^\circ$ , (111) plane, was not used for the calculation, since it is partially overlapped with the peak at  $2\theta = 44.83^\circ$ , (400) plane, of  $\text{MgAl}_2\text{O}_4$  phase. Field emission transmission electron microscopy (FE-TEM) analysis was performed using the JEM-2100F (JEOL, Tokyo, Japan) at 200 kV at the National Nanofab Center (NNFC). The nickel particle size distributions were estimated from randomly selected 100 particles in each TEM image by using the ImageJ software, version 1.8.0. Brunauer–Emmett–Teller (BET) analysis was carried out using BELSORP-mini (MicrotracBEL, Osaka, Japan). The samples were subjected to nitrogen adsorption and desorption at  $-196^\circ\text{C}$  after pretreatment in a vacuum at 300 °C for 3 h. The pore size distribution was analyzed according to the Barrett-Joyner-Halenda (BJH) theory. A  $\text{CO}_2$ -temperature-programmed desorption ( $\text{CO}_2$ -TPD) analysis was carried out using the AutoChem 2920 (Micromeritics, Norcross, GA, USA) under an He atmosphere at 300 °C for 2 h and  $\text{CO}_2$  adsorption at 40 °C for 1 h, followed by heating to 800 °C at a ramping rate of 5 °C/min. The reduction characteristics of the catalysts were analyzed by hydrogen temperature programmed reduction ( $\text{H}_2$ -TPR) using the BET-CAT (MicrotracBEL, Osaka, Japan). In the  $\text{H}_2$ -TPR measurement, about 150 mg of samples were loaded and heated (5 °C/min) in a gas flow (30 mL/min) containing a mixture of  $\text{H}_2$ :Ar (20:80). Prior to the  $\text{H}_2$ -TPR experiment, the samples were pretreated under an inert atmosphere (Ar) at 200 °C for 2 h and then cooled to room temperature. Thermogravimetric analysis with differential scanning calorimetry (TGA-DSC) analysis was performed using the Labsys TGA EVO (Setaram Instrumentation, Lyon, France) at temperatures up to 1400 °C in air. Inductive coupling plasma atomic emission spectroscopy (ICP-AES) analysis was performed to determine the chemical composition of the synthesized catalysts by using an Avio500 (Perkin-Elmer, Norwalk, MA, USA) after the pretreatment of dissolving catalysts in acidic digestion.

### 3.4. Catalyst Activity Test of SMR

For the catalytic reaction, the synthesized catalysts were ground and sieved using mesh (150–180  $\mu\text{m}$ ). As a reference catalyst, the Ni-based commercial steam reforming catalyst (Tablet type) was crushed, ground, and sieved with the same mesh mentioned above. The catalytic reaction was performed in a microreactor (a quartz tube of 1/4 inch inner diameter). The temperature was controlled by a digital program controller (KP1000, CHINO, Japan), while the influx of reactants was controlled by a mass flow controller (5850E, Brooks®, Halfield, PA, USA). The temperature difference between inside of the catalyst bed and outside of the reactor was measured, as shown in Supplementary Table S3. For the steam, distilled water heated to 180 °C was supplied by micro pump (NP-KX-200, DONGSUNG Science, Seoul, Korea). A K-type thermocouple was inserted into the reaction tube to measure the temperature of the catalyst bed. In the quartz reactor, 85 mg of catalyst was positioned between quartz wool. Reduction of the catalyst was performed under 50 sccm of 20 mol%  $\text{H}_2/\text{N}_2$  mixed gas at 900 and 550 °C for the developed catalysts and the commercial catalyst, respectively (by following the instructions for optimum reduction conditions). The reactions were performed under gas velocities

(Gas Hourly Space Velocity, GHSV =  $\text{h}^{-1}$ ) of 8000, 16,000, and 24,000  $\text{h}^{-1}$  at 800 °C at the steam to carbon (S/C) ratio of 3. In addition, the harsh condition reactions were performed at the S/C ratio of 1 under a space velocity GHSV of 8000  $\text{h}^{-1}$  at 700 °C. He was used as the carrier gas, and the outlet gas ( $\text{CH}_4$ , CO, and  $\text{CO}_2$ ) was analyzed using the TCD column of the HP 6890 GC system (Agilent Technologies Inc., Santa Clara, CA, USA) every 22 min. after stabilization of the catalytic reaction for 1 h. The performance of each catalyst was determined by  $\text{CH}_4$  conversion in consideration of a carbon balance of over 0.9.

#### 4. Conclusions

The mesoporous Ni/Mg-aluminate spinel catalysts were developed by synthesizing mesoporous Mg-aluminate supports with various Mg contents using the EISA method, followed by loading Ni active sites by the impregnation method. The Mg content affects the pore structures and the Ni particle sizes of the catalysts by changing the sintering resistance and the extent of the exsolution. The higher specific surface area with smaller pore size and smaller Ni particle size, which could be advantageous for the coke resistance, were obtained with the lower Mg contents. Nevertheless, the coke formation was mainly influenced by the basicity of the catalyst, and therefore the catalysts with the higher Mg contents showed stronger resistance against coke formation.

**Supplementary Materials:** The following are available online at <http://www.mdpi.com/2073-4344/10/8/828/s1>, Figure S1: TEM images of mesoporous Mg-aluminate calcined at 600 °C: (a,e) Mg9, (b,f) Mg19, (c,g) Mg25, (d,h) Mg30, Figure S2: TGA-DSC analysis of catalysts after reaction under harsh conditions: (a) Ni/Mg9, (b) Ni/Mg19, (c) Ni/Mg25, and (d) Ni/Mg30, Table S1: Pore structure analysis of mesoporous Mg-aluminate supports, after Ni loading with calcination and after reduction, Table S2: JCPDS card information of main peaks, Table S3: The temperature difference between inside of the catalyst bed and outside of the reactor during the reaction.

**Author Contributions:** Conceptualization, K.L. and Y.-H.L.; methodology, H.K., Y.-H.L., H.L., and J.-C.S.; validation, H.K. and H.L.; formal analysis, H.L. and J.-C.S.; investigation, H.K. and Y.-H.L.; data curation, H.L. and J.-C.S.; writing—original draft preparation, H.K. and Y.-H.L.; writing—review and editing, K.L.; supervision, K.L.; funding acquisition, K.L. All authors have read and agreed to the published version of the manuscript.

**Funding:** This research was funded by the framework of the research and development program of the Korea Institute of Energy Research (C0-2406). This research was also supported by two National Research Foundation of Korea (NRF) grants (NRF-2020R1A2C1009054 and NRF-2020R1A4A2002590).

**Conflicts of Interest:** The authors declare no conflict of interest.

#### References

1. Møller, K.T.; Jensen, T.R.; Akiba, E.; Li, H.-w. Hydrogen—A sustainable energy carrier. *Pro. Nat. Sci. Mater.* **2017**, *27*, 34–40. [[CrossRef](#)]
2. The Future of Hydrogen—Analysis-IEA. Available online: <https://webstore.iea.org/the-future-of-hydrogen> (accessed on 30 May 2020).
3. Mei, D.; Glezakou, V.-A.; Lebarbier, V.; Kovarik, L.; Wan, H.; Albrecht, K.O.; Gerber, M.; Rousseau, R.; Dagle, R.A. Highly active and stable  $\text{MgAl}_2\text{O}_4$ -supported Rh and Ir catalysts for methane steam reforming: A combined experimental and theoretical study. *J. Catal.* **2014**, *316*, 11–23. [[CrossRef](#)]
4. Watanabe, F.; Kaburaki, I.; Shimoda, N.; Satokawa, S. Influence of nitrogen impurity for steam methane reforming over noble metal catalysts. *Fuel Process. Technol.* **2016**, *152*, 15–21. [[CrossRef](#)]
5. Kikuchi, E.; Tanaka, S.; Yamazaki, Y.; Morita, Y. Steam reforming of hydrocarbons on noble metal catalysts (part 1). *J. Jpn. Pet. Inst.* **1974**, *16*, 95–98. [[CrossRef](#)]
6. Jones, G.; Jakobsen, J.G.; Shim, S.S.; Kleis, J.; Andersson, M.P.; Rossmesl, J.; Abild-Pedersen, F.; Bligaard, T.; Helveg, S.; Hinnemann, B.; et al. First principles calculations and experimental insight into methane steam reforming over transition metal catalysts. *J. Catal.* **2008**, *259*, 147–160. [[CrossRef](#)]
7. Trimm, D.L. Coke formation and minimisation during steam reforming reactions. *Catal. Today* **1997**, *37*, 233–238. [[CrossRef](#)]
8. Sehested, J. Sintering of nickel steam-reforming catalysts. *J. Catal.* **2003**, *217*, 417–426. [[CrossRef](#)]

9. Li, S.; Gong, J. Strategies for improving the performance and stability of Ni-based catalysts for reforming reactions. *Chem. Soc. Rev.* **2014**, *43*, 7245–7256. [[CrossRef](#)]
10. Liu, C.J.; Ye, J.; Jiang, J.; Pan, Y. Progresses in the preparation of coke resistant Ni-based catalyst for steam and CO<sub>2</sub> reforming of methane. *ChemCatChem* **2011**, *3*, 529–541. [[CrossRef](#)]
11. Kehres, J.; Jakobsen, J.G.; Andreasen, J.W.; Wagner, J.B.; Liu, H.; Molenbroek, A.; Sehested, J.; Chorkendorff, I.; Vegge, T. Dynamical properties of a Ru/MgAl<sub>2</sub>O<sub>4</sub> catalyst during reduction and dry methane reforming. *J. Phys. Chem.* **2012**, *116*, 21407–21415. [[CrossRef](#)]
12. Gonzalez-DelaCruz, V.M.; Holgado, J.P.; Pereñíguez, R.; Caballero, A. Morphology changes induced by strong metal–support interaction on a Ni-ceria catalytic system. *J. Catal.* **2008**, *257*, 307–314. [[CrossRef](#)]
13. Ewbank, J.L.; Kovarik, L.; Diallo, F.Z.; Sievers, C. Effect of metal–support interactions in Ni/Al<sub>2</sub>O<sub>3</sub> catalysts with low metal loading for methane dry reforming. *Appl. Catal. A Gen.* **2015**, *494*, 57–67. [[CrossRef](#)]
14. Zhai, X.; Ding, S.; Liu, Z.; Jin, Y.; Cheng, Y. Catalytic performance of Ni catalysts for steam reforming of methane at high space velocity. *Int. J. Hydrogen Energy* **2011**, *36*, 482–489. [[CrossRef](#)]
15. Jang, W.-J.; Shim, J.-O.; Kim, H.-M.; Yoo, S.-Y.; Roh, H.-S. A review on dry reforming of methane in aspect of catalytic properties. *Catal. Today* **2019**, *324*, 15–26. [[CrossRef](#)]
16. Han, J.W.; Park, J.S.; Choi, M.S.; Lee, H. Uncoupling the size and support effects of Ni catalysts for dry reforming of methane. *Appl. Catal. B Environ.* **2017**, *203*, 625–632. [[CrossRef](#)]
17. Koo, K.Y.; Roh, H.-S.; Seo, Y.T.; Seo, D.J.; Yoon, W.L.; Park, S.B. Coke study on MgO-promoted Ni/Al<sub>2</sub>O<sub>3</sub> catalyst in combined H<sub>2</sub>O and CO<sub>2</sub> reforming of methane for gas to liquid (GTL) process. *Appl. Catal. A Gen.* **2008**, *340*, 183–190. [[CrossRef](#)]
18. Koo, K.Y.; Roh, H.-S.; Seo, Y.T.; Seo, D.J.; Yoon, W.L.; Park, S.B. A highly effective and stable nano-sized Ni/MgO–Al<sub>2</sub>O<sub>3</sub> catalyst for gas to liquids (GTL) process. *Int. J. Hydrogen Energy* **2008**, *33*, 2036–2043. [[CrossRef](#)]
19. Jabbour, K.; Massiani, P.; Davidson, A.; Casale, S.; El Hassan, N. Ordered mesoporous “one-pot” synthesized Ni-Mg (Ca)-Al<sub>2</sub>O<sub>3</sub> as effective and remarkably stable catalysts for combined steam and dry reforming of methane (CSDRM). *Appl. Catal. B Environ.* **2017**, *201*, 527–542. [[CrossRef](#)]
20. Alipour, Z.; Rezaei, M.; Meshkani, F. Effect of Ni loadings on the activity and coke formation of MgO-modified Ni/Al<sub>2</sub>O<sub>3</sub> nanocatalyst in dry reforming of methane. *J. Energy Chem.* **2014**, *23*, 633–638. [[CrossRef](#)]
21. Zhang, C.; Zhu, W.; Li, S.; Wu, G.; Ma, X.; Wang, X.; Gong, J. Sintering-resistant Ni-based reforming catalysts obtained via the nanoconfinement effect. *ChemComm* **2013**, *49*, 9383–9385. [[CrossRef](#)]
22. Dehghan-Niri, R.; Walmsley, J.C.; Holmen, A.; Midgley, P.A.; Rytter, E.; Dam, A.H.; Hungria, A.B.; Hernandez-Garrido, J.C.; Chen, D. Nanoconfinement of Ni clusters towards a high sintering resistance of steam methane reforming catalysts. *Catal. Sci. Technol.* **2012**, *2*, 2476–2484. [[CrossRef](#)]
23. Ganesh, I. A review on magnesium aluminate (MgAl<sub>2</sub>O<sub>4</sub>) spinel: Synthesis, processing and applications. *Int. Mater. Rev.* **2013**, *58*, 63–112. [[CrossRef](#)]
24. Katheria, S.; Gupta, A.; Deo, G.; Kunzru, D. Effect of calcination temperature on stability and activity of Ni/MgAl<sub>2</sub>O<sub>4</sub> catalyst for steam reforming of methane at high pressure condition. *Int. J. Hydrogen Energy* **2016**, *41*, 14123–14132. [[CrossRef](#)]
25. Sehested, J.; Carlsson, A.; Janssens, T.; Hansen, P.; Datye, A. Sintering of nickel steam-reforming catalysts on MgAl<sub>2</sub>O<sub>4</sub> spinel supports. *J. Catal.* **2001**, *197*, 200–209. [[CrossRef](#)]
26. Abdullah, B.; Ghani, N.A.A.; Vo, D.-V.N. Recent advances in dry reforming of methane over Ni-based catalysts. *J. Clean. Prod.* **2017**, *162*, 170–185. [[CrossRef](#)]
27. Li, D.; Lu, M.; Cai, Y.; Cao, Y.; Zhan, Y.; Jiang, L. Synthesis of high surface area MgAl<sub>2</sub>O<sub>4</sub> spinel as catalyst support via layered double hydroxides-containing precursor. *Appl. Clay Sci.* **2016**, *132*, 243–250. [[CrossRef](#)]
28. Christensen, K.O.; Chen, D.; Lodeng, R.; Holmen, A. Effect of supports and Ni crystal size on carbon formation and sintering during steam methane reforming. *Appl. Catal. A Gen.* **2006**, *314*, 9–22. [[CrossRef](#)]
29. Yang, Q.; Zhenmin, C.; Zhiming, Z. Steam reforming of methane over Ni catalysts prepared from hydrotalcite-type precursors: Catalytic activity and reaction kinetics. *Chin. J. Chem. Eng.* **2015**, *23*, 76–85.
30. Weihua, S.; Kenta, K.; Tomaya, H.; Akihiro, Y.; Shuichi, N. Steam reforming of methane over ordered mesoporous Ni-Mg-Al oxides. *Chem. Commun.* **2009**, *42*, 6490–6492.

31. Habibi, N.; Arandiyani, H.; Rezaei, M. Mesoporous MgO·Al<sub>2</sub>O<sub>3</sub> nanopowder-supported meso–macroporous nickel catalysts: A new path to high-performance biogas reforming for syngas. *RSC Adv.* **2016**, *6*, 29576–29585. [[CrossRef](#)]
32. Hadian, N.; Rezaei, M.; Mosayebi, Z.; Meshkani, F. CO<sub>2</sub> reforming of methane over nickel catalysts supported on nanocrystalline MgAl<sub>2</sub>O<sub>4</sub> with high surface area. *J. Nat. Gas Chem.* **2012**, *21*, 200–206. [[CrossRef](#)]
33. Xu, L.; Wang, F.; Chen, M.; Yang, H.; Nie, D.; Qi, L.; Lian, X. Alkaline-promoted Ni based ordered mesoporous catalysts with enhanced low-temperature catalytic activity toward CO<sub>2</sub> methanation. *RSC Adv.* **2017**, *7*, 18199–18210. [[CrossRef](#)]
34. Cho, E.; Lee, Y.; Kim, H.; Jang, E.J.; Kwak, J.H.; Lee, K.; Ko, C.H.; Yoon, W.L. Ni Catalysts for Dry Methane Reforming Prepared by A-site Exsolution on Mesoporous Defect Spinel Magnesium Aluminate. *Appl. Catal. A Gen.* **2020**, *602*, 117694. [[CrossRef](#)]
35. Dong, G.; Ferdi, S. Synthesis of non-siliceous mesoporous oxide. *Chem. Soc. Rev.* **2014**, *43*, 313–344.
36. Basso, R.; Carbonin, S.; Della Giusta, A. Cation and vacancy distribution in a synthetic defect spinel. *Z. Kristallogr. Cryst. Mater.* **1991**, *194*, 111–120. [[CrossRef](#)]
37. Zubenko, D.; Singh, S.; Rosen, B.A. Exsolution of Re-alloy catalysts with enhanced stability for methane dry reforming. *Appl. Catal. B Environ.* **2017**, *209*, 711–719. [[CrossRef](#)]
38. Zeng, D.; Qiu, Y.; Peng, S.; Chen, C.; Zeng, J.; Zhang, S.; Xiao, R. Enhanced hydrogen production performance through controllable redox exsolution within CoFeAlO<sub>x</sub> spinel oxygen carrier materials. *J. Mater. Chem. A* **2018**, *6*, 11306–11316. [[CrossRef](#)]
39. Oh, J.H.; Kwon, B.W.; Cho, J.; Lee, C.H.; Kim, M.K.; Choi, S.H.; Yoon, S.P.; Han, J.; Nam, S.W.; Kim, J.Y. Importance of Exsolution in Transition-Metal (Co, Rh, and Ir)-Doped LaCrO<sub>3</sub> Perovskite Catalysts for Boosting Dry Reforming of CH<sub>4</sub> Using CO<sub>2</sub> for Hydrogen Production. *Ind. Eng. Chem. Res.* **2019**, *58*, 6385–6393. [[CrossRef](#)]
40. Nguyen, T.H.; Łamacz, A.; Krztoń, A.; Liszka, B.; Djéga-Mariadassou, G. Partial oxidation of methane over Ni<sup>0</sup>/La<sub>2</sub>O<sub>3</sub> bifunctional catalyst III. Steady state activity of methane total oxidation, dry reforming, steam reforming and partial oxidation. Sequences of elementary steps. *Appl. Catal. B Environ.* **2016**, *182*, 385–391. [[CrossRef](#)]
41. Foo, S.Y.; Cheng, C.K.; Nguyen, T.-H.; Adesina, A.A. Evaluation of lanthanide-group promoters on Co–Ni/Al<sub>2</sub>O<sub>3</sub> catalysts for CH<sub>4</sub> dry reforming. *J. Mol. Catal. A Chem.* **2011**, *344*, 28–36. [[CrossRef](#)]
42. Smoláková, L.; Frolich, K.; Troppová, I.; Kutálek, P.; Kroft, E.; Čapek, L. Determination of basic sites in Mg–Al mixed oxides by combination of TPD-CO<sub>2</sub> and CO<sub>2</sub> adsorption calorimetry. *J. Therm. Anal. Calorim.* **2017**, *127*, 1921–1929. [[CrossRef](#)]



© 2020 by the authors. Licensee MDPI, Basel, Switzerland. This article is an open access article distributed under the terms and conditions of the Creative Commons Attribution (CC BY) license (<http://creativecommons.org/licenses/by/4.0/>).